Solid-State Electronics 193 (2022) 108269

Contents lists available at ScienceDirect

Solid State Electronics

journal homepage: www.elsevier.com/locate/sse

Temperature increase in STT-MRAM at writing: A fully three-dimensional finite element approach

T. Hadámek [a,*], S. Fiorentini [a], M. Bendra [a,b], J. Ender [a,b], R.L. de Orio [b], W. Goes [c], S. Selberherr [b], V. Sverdlov [a]

[a] Christian Doppler Laboratory for Nonvolatile Magnetoresistive Memory and Logic at the Institute for Microelectronics, Austria
[b] Institute for Microelectronics, TU Wien, Gußhausstraße 27-29/E360, 1040 Vienna, Austria
[c] Silvaco Europe Ltd., Cambridge, United Kingdom

ARTICLE INFO

Keywords:
STT-MRAM
Magnetic tunnel junction
Current-induced heating
Non-uniform temperature
Temperature variations

ABSTRACT

The writing process in spin transfer torque magnetoresistive random access memories (STT-MRAM) is facilitated by elevated temperatures. In this work we investigate the temperature distribution and development in the free layer (FL) of an STT-MRAM during switching. With our fully three-dimensional (3D) finite element method simulation approach, we numerically solve the heat transport equation coupled to the electron, spin, and magnetization dynamics and demonstrate that the FL temperature is highly inhomogeneous due to the non-uniform magnetization of the FL during switching for an STT-MRAM with large magnetic tunnel junction (MTJ) diameter. While the average temperature in the FL can be obtained based on an average current density and an averaged potential drop across the tunnel barrier, a fully 3D model is required to evaluate the large local temperature variations. The temperature variations in the FL further increase, when realistic device structures with an MTJ coated by a passivation layer and contacted to broad electrodes are considered. Lowering the FL thermal conductivity increases the temperature variations even further. However, the variations are strongly reduced with the decrease of the MTJ diameter.

1. Introduction

The ongoing miniaturization of semiconductor components has pushed the chip technology to its limits due to rapidly increasing leakage currents. Moreover, in the commonly employed von Neumann architecture, where the processing unit is separated from the memory, significant energy losses due to the data transfer back and forth, the so called von Neumann bottleneck, exist. The magnetoresistive random access memory (MRAM) is a promising emerging candidate to overcome these issues. MRAM is complementary metal-oxide semiconductor (CMOS) compatible [1–3] and has zero stand-by power consumption as it is intrinsically nonvolatile. It can also be integrated into logic [4], offers a wide temperature operation range [5], and has very good endurance.

A magnetic tunnel junction (MTJ), the basic building block of MRAM cells, consists of three layers: a pinned ferromagnetic layer, an oxide barrier, and a free ferromagnetic layer (FL). In spin-transfer torque MRAM (STT-MRAM) [6], relatively high current densities through the structure are required to switch the magnetization of the FL. This results in an increased temperature of the STT-MRAM cell, which mediates the switching of the FL magnetization [7,8]. On the other hand, the increased FL temperature caused by self-heating can result in an information loss, as it compromises the thermal stability [8]. To preserve the data, the temperature must be rapidly relaxed after writing. In [9], a heating asymmetry in the MTJ was observed for reversed current direction. This asymmetry was further numerically studied in [10], showing a non-linear increase of the saturation temperature with increasing power.

In this work we investigate the inhomogeneity of the temperature in the FL during switching. This inhomogeneity can be expected due to the fast magnetization dynamics of the STT-MRAM cell, which results in a significant inhomogeneity of the current density across the FL plane caused by a non-uniform magnetization [11–14]. Moreover, during switching, the current densities change significantly due to the rapid dynamics of the magnetization direction. Therefore, to model the temperature in STT-MRAM, the heat transport must be coupled to current,

* Corresponding author.
E-mail address: hadamek@iue.tuwien.ac.at (T. Hadámek).

https://doi.org/10.1016/j.sse.2022.108269

Available online 2 March 2022
0038-1101/© 2022 The Authors. Published by Elsevier Ltd. This is an open access article under the CC BY license (http://creativecommons.org/licenses/by/4.0/).

magnetization, and spin dynamics in a fully three-dimensional (3D) model. To the authors' knowledge, full 3D simulations coupling temperature, spin, and magnetization dynamics of STT-MRAM during switching have not been performed. The previous studies utilize either a simple one-dimensional (1D) model [15] for the heat or employ power (current) averaging over the barrier [7]. This manuscript is a follow-up article of a previously published conference contribution [16], which extends the previously published work to more realistic structures with broadened contacts and an oxide passivation layer, and investigates the effects of lower FL thermal conductivity and longer STT-MRAM contacts.

In Section 2, the general model used to simulate temperature, magnetization and spin dynamics is introduced together with the simulated structures and used parameters. Section 3 presents and discusses results from switching simulations under a constant voltage applied on the STT-MRAM cell. Temperature profiles of the FL for different structures are shown and analyzed. Section 4 summarizes the findings of this work.

2. Method

2.1. Temperature modelling

To describe the dynamics of the temperature T in the structure at time t and position $\boldsymbol{r}$, the heat flow equation is used.

$$c_v\rho\frac{\partial T(\boldsymbol{r},t)}{\partial t}-\nabla\cdot[\kappa\nabla T(\boldsymbol{r},t)]=q(\boldsymbol{r},t) \tag{1}$$

c_v, ρ, and κ stand for the heat capacity, mass density, and heat conductivity of the material, respectively. q is the heat source term. In MTJs, two main heat sources can be identified.

The first heat source is attributed to the Joule heating in the ferromagnetic layers and in the metal contacts. It can be expressed as: $q_r(\boldsymbol{r},t)=\boldsymbol{j}^2(\boldsymbol{r},t)\rho_E$, where ρ_E is the material resistivity and $\boldsymbol{j}$ is the current density.

The second heat source is associated with electrons tunneling through the insulating barrier [7,8]. When a potential difference is applied across the MTJ, an electron starts tunneling from the low potential side (source) and arrives at the high potential side (receiver) as a hot electron. Its energy is above the receiver Fermi energy and must be dissipated through various scattering processes. Similarly, the hole left behind the electron at the source must be filled by an electron from a higher energy level, the excess energy of which is therefore released. Setting the x-axis to coincide with the main axis along the structure, the hot electron/hole heat source is described by [10].

$$q_t(\boldsymbol{r},t)=(1\pm\alpha(\Delta U))\frac{j_x(y,z,t)\Delta U(y,z,t)}{2\lambda}\exp\left(-\frac{|x-x_{F/P}|}{\lambda}\right), \tag{2}$$

where j_x and ΔU stand for the x-component of the current density and the potential drop at the position (y,z) along the FL plane. The x-coordinate of the position of the free/pinned-barrier interface is denoted by $x_{F/P}$ and λ is a characteristic length at which hot electrons/holes lose their energy. The heat production imbalance between the receiver and the source side is accounted for by the asymmetry coefficient $\alpha(\Delta U)$ [10]. In this work α is set to zero – no asymmetry between the receiver and source sides is considered – in order to fully investigate the details of inhomogeneous temperature development due to the non-uniform current density. The system relevant parameters are listed in Tables 1 and 2.

2.2. Magnetization dynamics modelling

To describe the magnetization dynamics in the micromagnetic model the Landau-Lifshitz-Gilbert (LLG) equation is used.

Table 1
Simualtion Parameters – Heat.

	MgO	CoFeB	NM	PL
ρ [kg m^{-3}]	3600	8200	8050	2130
c_v [J K^{-1} kg^{-1}]	735	440	500	650^{B}
κ [W K^{-1} m^{-1}]	0.38^{A}	83	43	1.1^{B}
ρ_e [Ωm]	–	2×10^{-5}	2×10^{-5}	–
λ [nm]	–	1	1	–

A. Taken from [15].
B. Taken from [17].

Table 2
Simualtion Parameters – Magnetization and Spin.

Parameter	Value
Gilbert damping, α	0.02
Gyromagnetic ratio, γ	$1.76\cdot10^{11}$ rad s^{-1} T^{-1}
Saturation magnetization, M_S	$1.2\cdot10^{6}$ A m^{-1}
Exchange constant, A	$1\cdot10^{-11}$ J m^{-1}
Anisotropy constant, K	$0.9\cdot10^{6}$ J m^{-3}
Current spin polarization, β_σ	0.7
Diffusion spin polarization, β_D	1.0
Electron diffusion coefficient, D_e	$1\cdot10^{-4}$ m^2/s
Spin-flip length, λ_{sf}	10 nm
Spin dephasing length, λ_φ	5 nm
Exchange length, λ_J	0.5 nm
Tunnel megnetoresistance ratio (TMR)	200%

$$\frac{\partial\boldsymbol{m}}{\partial t}=-\gamma\mu_0\boldsymbol{m}\times\boldsymbol{H}_{\rm eff}+\alpha\boldsymbol{m}\times\frac{\partial\boldsymbol{m}}{\partial t}+\frac{1}{M_S}\boldsymbol{T}_S. \tag{3}$$

Here $\boldsymbol{m}$ is the normalized magnetization, $\gamma\mu_0$ is the scaled gyromagnetic ratio, α is the Gilbert damping, and M_S stands for the saturation magnetization. The effective field $\boldsymbol{H}_{\rm eff}$ consists of several components, with the demagnetization field$\boldsymbol{H}_{\rm demag}$, the anisotropy field $\boldsymbol{H}_{\rm aniso}$ and the exchange field $\boldsymbol{H}_{\rm ex}$ contributing the most. In the following, $\boldsymbol{H}_{\rm demag}$ is determined by an optimized hybrid FEM-BEM approach [18], and $\boldsymbol{H}_{\rm aniso}$ and $\boldsymbol{H}_{\rm ex}$ are calculated with the parameters listed in Table 2. $\boldsymbol{T}_S$ stands for the STT exerted by the spin current on the magnetization. To determine$\boldsymbol{T}_S$, the spin accumulation in the structure is computed [11,13]. The current densities and potentials within the structure, further used in the heat simulations, are determined by solving the coupled spin, charge, and magnetization dynamics in an MTJ [12].

The two main approaches to include temperature in the LLG equation introduce scaling of M_S with temperature [19] or a random thermal field contribution to $\boldsymbol{H}_{\rm eff}$ [20]. The former seems not to be suited for STT-MRAM modelling as the switching remains deterministic, therefore, it is not fully usable for statistical switching simulations of STT-MRAM as it does not represent the correct dynamics of the system. The latter requires a careful temperature rescaling to account for the mesh size [20]. This method mainly reduces the incubation phase and introduces thermal fluctuations to the system, but does not have significant effects during the main switching phase. Therefore, the coupling of temperature to the LLG was omitted as the focus of the work is the FL temperature profile which is not significantly affected by the random thermal field inclusion.

The described approach was implemented in a fully 3D finite element method solver based on an open-source library MFEM [21]. For the time integration, an implicit Euler method was used.

2.3. Simulated structures

For the simulations, three different structures were considered. In Fig. 1, a simplified mesh of a cylindrical five-layer STT-MRAM structure is shown. The three-layer MTJ stack consisting of CoFeB(1 nm)/MgO(1 nm)/CoFeB(1.2 nm) is connected to non-magnetic metal (NM) contacts

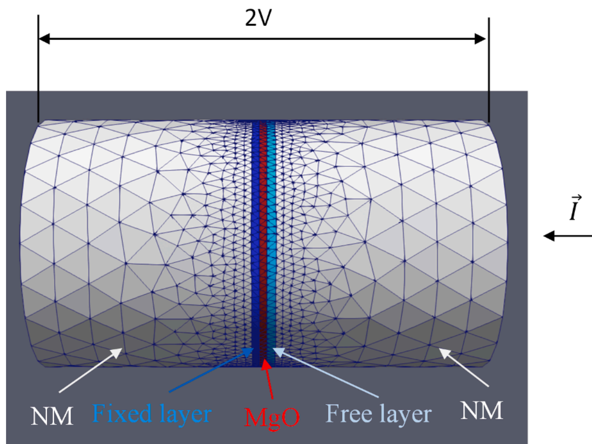

Fig. 1. Simplified mesh of the first simulated structure. The 5-layer structure consists of CoFeB(1 nm)/MgO(1 nm)/CoFeB(1.2 nm) MTJ connected to normal metal contacts (30 nm). The diameter is 40 nm. Both contact ends are kept at a constant temperature. A bias of 2 V is applied across the structure.

(30 nm). Both contact ends are kept at a constant temperature. No heat transfer is assumed across the shell of the cylinder. The structure diameter is 40 nm.

In a real device, the MTJ stack is connected to wider contacts and is surrounded by an oxide passivation layer [15,22]. Fig. 2 shows such a structure with broadened contacts and SiO_2 serving as the passivation layer (yellow). The contacts consist of three different regions: 20 nm tall cylinder with a diameter of 200 nm, 10 nm tall conical tapering, and a 20 nm tall cylinder with a diameter of 40 nm. The MTJ diameter is again 40 nm (same layer color coding as in Fig. 1). The hollow space between the broadened contacts is filled with SiO_2. There is no heat transfer assumed across the shell of the outer cylinder and both ends are kept at constant temperature (top and bottom of the structure in Fig. 2). The third structure is identical to one in Fig. 2, but the MTJ and the narrow contact ends have a smaller diameter of 20 nm.

3. Results

When a voltage is applied to the ends of the contacts, an electric current starts to flow through the structure, exerting an STT on the FL magnetization. For a high enough voltage, the FL magnetization is eventually flipped. In the simulations, 2 V and −2 V between the contacts were applied to achieve a reliable parallel to anti-parallel (P-AP) and anti-parallel to parallel (AP-P) switching, respectively. We first consider the structure shown in Fig. 1. The averages of the magnetization components of the FL for P-AP (AP-P) at switching are displayed in Fig. 3 in the left (right) panel. In both plots, three different switching regions can be identified: Initial oscillations of the magnetization in the *y-z* plane, fast *x* magnetization component (m_x) change, and final magnetization oscillation in the *y-z* plane. While the fast m_x changes are comparable for both P-AP and AP-P switching, the initial and final oscillatory phases vary significantly. In the P-AP switching, the initial (final) oscillations are much longer (shorter) lasting than for the AP-P switching. In both simulations, the FL magnetization is tilted by 5° from the easy axis to eliminate the slow incubation phase.

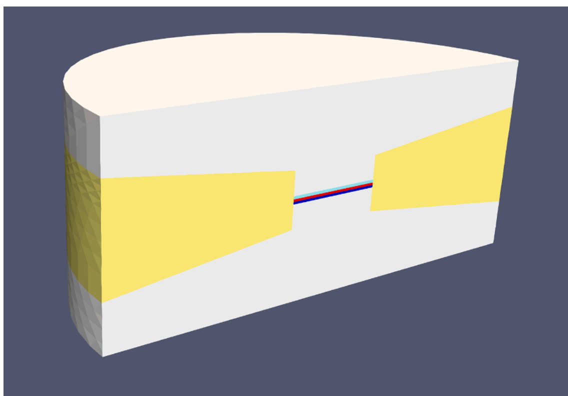

Fig. 2. Cylindrical MRAM structure with broadened contacts and a passivation layer. The MTJ stack with a diameter of 40 nm is shown in the middle, passivation layer is depicted in yellow and contacts in white. The wider contact diameter is 200 nm. The top and the bottom surfaces of the contacts are kept at a constant temperature, no heat transfer is assumed across the walls of the cylinder. (For interpretation of the references to color in this figure legend, the reader is referred to the web version of this article.)

Fig. 4 shows the FL temperature increase development for P-AP (left panel) and AP-P (right panel). The contact end temperature is set to 300 K. In the following, we refer to the temperature increase of the FL above the end contact temperature as the temperature of the FL, but indicate it with δT to prevent any confusion. The average temperature δT_{avg} (solid green), the minimum temperature δT_{min} (dot-dashed gray), and the maximum temperature increase δT_{max} (dashed black) of the FL obtained from the fully 3D model are shown. The average temperature increase δT_{avg-1D} calculated with an average current density and an average potential drop across the barrier is also shown (dotted orange) and coincides with δT_{avg} from the 3D simulations. The fast initial heating phase (~150 ps), after which the FL temperature saturates for the given magnetization orientation, is followed by a slow temperature change due to dynamic magnetization behavior during switching. In the beginning, δT_{min} and δT_{max} nearly coincide. This indicates a homogeneous FL temperature profile. Later, δT_{min} and δT_{max} vary significantly and coincide again towards the end of the switching.

Fig. 5 shows the temperature profile (left) next to m_x (right) of the FL at 1 ns for the AP-P switching. The low (high) temperature region clearly correlates with the positive (negative) value region of m_x. The heating in the STT-MRAM during switching is dominated by the tunneling electrons/holes (ca. 93–96 % of the total heat produced).

Another correlation is found when comparing Fig. 3 to Fig. 4. The maximum temperature difference at the FL,$\Delta T_{max} \equiv \delta T_{max} - \delta T_{min}$, is significantly increased when oscillations in the *y-z* plane decrease. This is further visualized in Fig. 6, where the ratio of ΔT_{max} to δT_{avg} is shown. In both switching scenarios, P-AP and AP-P, this ratio exceeds 30% in the middle switching region. During the switching, δT_{avg} follows the increase of the average magnetization m_x with approximately a 20–60 ps delay.

The more realistic structures described in Section 2.3 with broadened contacts and the SiO_2 passivation layer are now considered. For AP-P switching, −2 V is again applied between the contacts and a switching comparable to Fig. 3 (right) is observed (not shown). The FL temperature in a cut through the center of the structure with the 40 nm MTJ at 1.75 ns is shown in Fig. 7. The warmest area is confined around the MTJ stack.

Fig. 8 shows the temperature development of the FL for the MTJ structure with a diameter of 40 nm and 20 nm, respectively. For the MTJ with the diameter of 40 nm (left plot), the general temperature behavior is similar to that observed for the simpler structure (Fig. 4). The main difference can be seen in the last switching phase, where δT_{max} and δT_{min} remain different, in contrast to the results for the simpler structure. This is due to the presence of the passivation layer. The edges of the FL are cooled and have lower temperatures than the FL center. For the MTJ with the diameter of 20 nm (right plot) the situation results are dramatically different. BothδT_{max},δT_{min}, and ΔT_{avg} nearly coincide. In this case, the MTJ is so narrow that even the cooled FL edges have almost identical temperature to the FL center. This fact is clearly reflected in Fig. 9, where the ratio of ΔT_{max} to δT_{avg} is shown for both structures. For the broad MTJ (left plot), ΔT_{max} exceeds 45% ofδT_{avg}. When the narrow MTJ is considered, the ratio ΔT_{max} to δT_{avg} stays below 5% for all

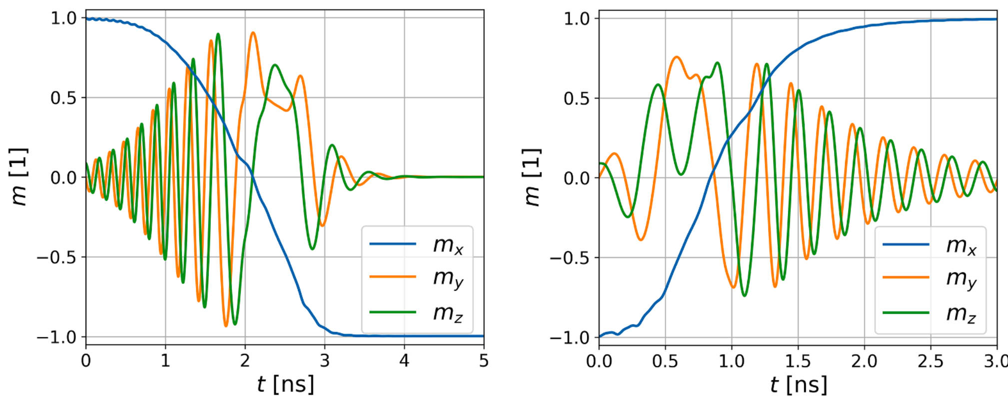

Fig. 3. Averages of the normalized FL magnetization in x-, y- and z-direction during switching for the structure in Fig. 1. The left (right) panel shows switching from the initial parallel to anti-parallel (anti-parallel to parallel) magnetic orientation. The parallel to anti-parallel switching shows a longer initial oscillating behaviour, whereas in the parallel to anti-parallel switching, strong oscillating behavior is visible at the final switching phase. The initial magnetization was tilted by 5° in the z-direction from the x-direction to eliminate the slow incubation phase.

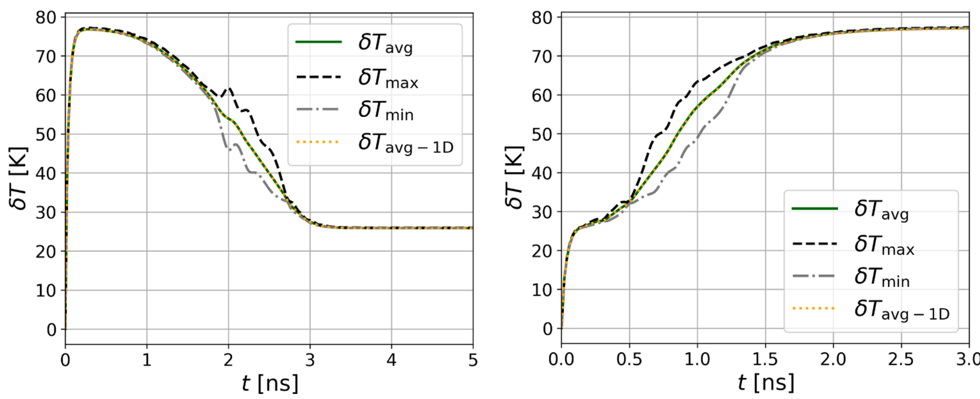

Fig. 4. Temperature in the FL during switching for the structure in Fig. 1. On the left (right) switching from the initial parallel to anti-parallel (anti-parallel to parallel) magnetic orientation is shown. An average temperature increase δT_{avg} (solid green), maximum temperature increase (dashed black), minimum temperature increase (dot-dashed grey) and δT_{avg-1D} (dotted orange, coincides with green) - calculated using averages of current densities and potential drop – are shown. All temperatures are displayed with respect to the ambient temperature (300 K). (For interpretation of the references to color in this figure legend, the reader is referred to the web version of this article.)

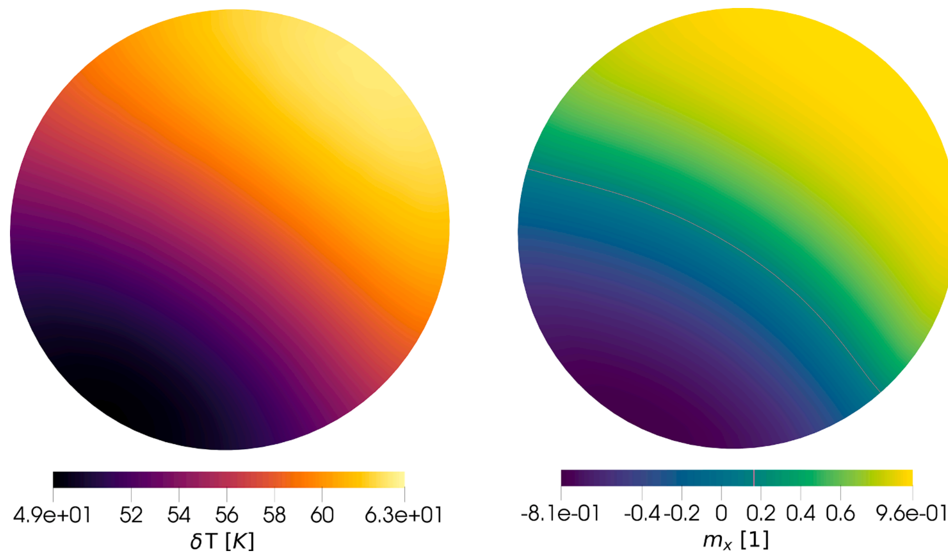

Fig. 5. Temperature profile (left) and m_x (right) in the FL at 1 ns during AP-P switching for the structure in Fig. 1. The minimum/maximum temperature region coincides with the minimum/maximum region ofm_x.

switching phases. Due the increased heat flux from the FL for both structures with the broadened contacts and the passivation layer, the initial saturation is reached faster (~100–120 ps) than for the simple scenario.

Now we consider lower thermal conductivity in the FL – 10 % of the original one – for the structure in Fig. 2. The rest of the parameters is kept unchanged. When the thermal conductivity is reduced, the temperature inhomogeneity further increases as show in the left plot in Fig. 10. The ratio of ΔT_{max} to δT_{avg} exceeds 50 % for the fast switching phase (not shown). As the last scenario we investigate the FL temperature dependence on the contact length. The left plot in Fig. 10 shows δT_{avg} of the FL at 4 ns (end of switching) for different lengths of the narrow part of the contacts of the structure in Fig. 2. δT_{avg} increases linearly with the increasing length of the contact. The linear fit crosses $l = 0$ nm at 32.4 K due to the remaining wide and tapered contact parts. ΔT_{max} did not show any clear trend and remained within ±1 K of the

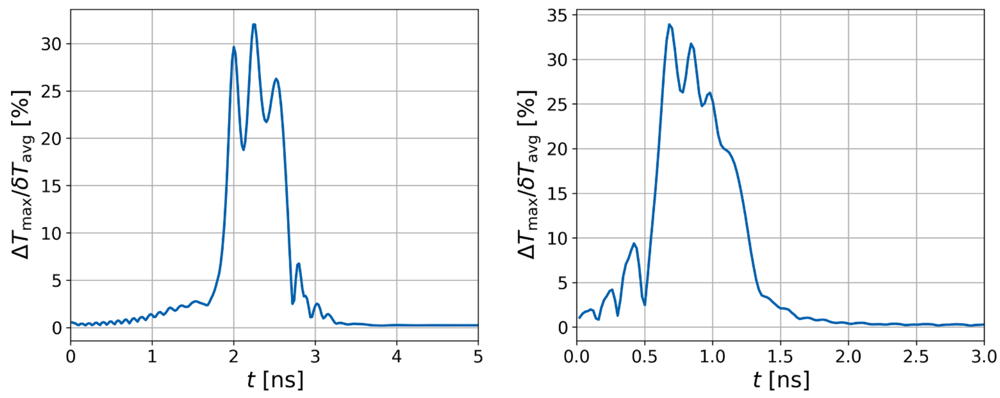

Fig. 6. Ratio of the maximum temperature difference ΔT_{max} of the FL to the average FL temperature increase δT_{avg} for the structure shown in Fig. 1. The left (right) panel shows switching from the initial parallel to anti-parallel (anti-parallel to parallel) state. ΔT_{max} exeeds 30 % of the average temperature, when m_y and m_z stop to oscillate.

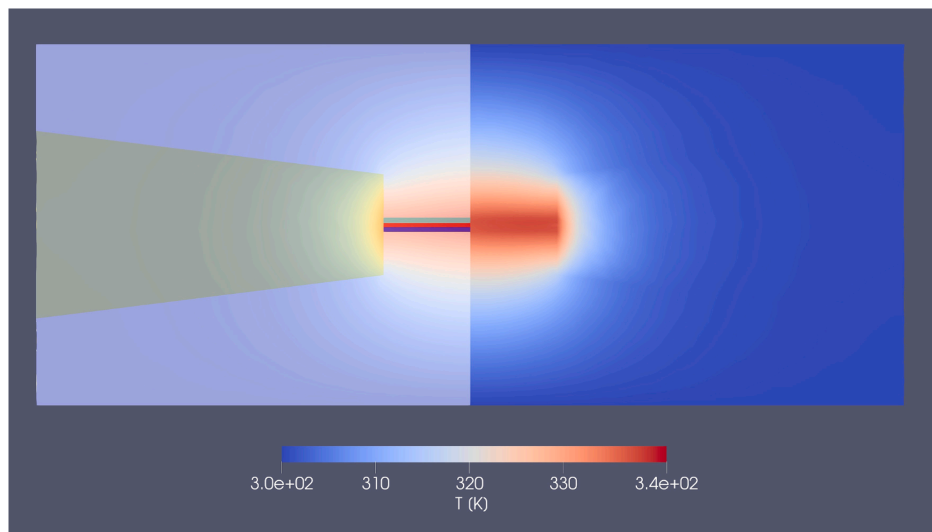

Fig. 7. Temperature profile of a structure with broadened contacts, MTJ with a diameter of 40 nm, and a SiO_2 passivation layer. The right side of the plot shows temperature of the structure true to the scale, left side shows temperature with partial transparency with the MRAM structure cut in the background. The top and bottom of the structure are kept at constant temperature (300 K).

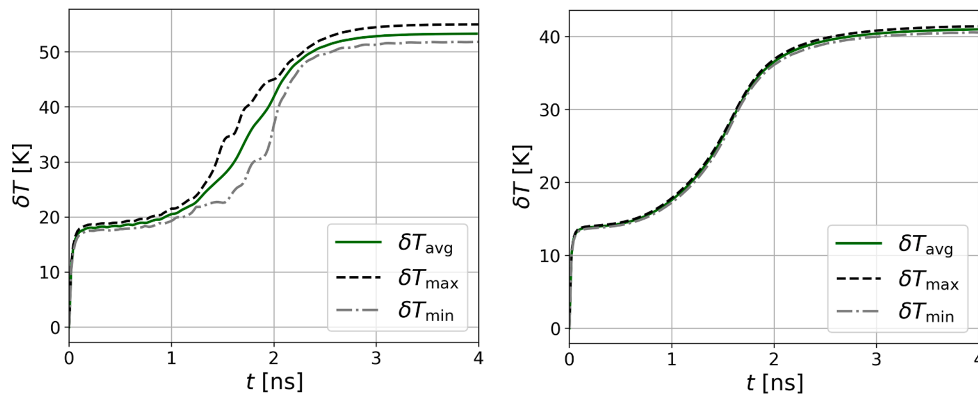

Fig. 8. FL temperature during anti-parallel to parallel switching for structures with broadened contacts and SiO_2 passivation layer. The temperature for the structure with MTJ diameter of 40 nm (20 nm) is show on the left (right) plot. The maximum and minimum temperature of the FL vary significantly during switching for the wide MTJ, whereas they almost coincide for the narrow MTJ.

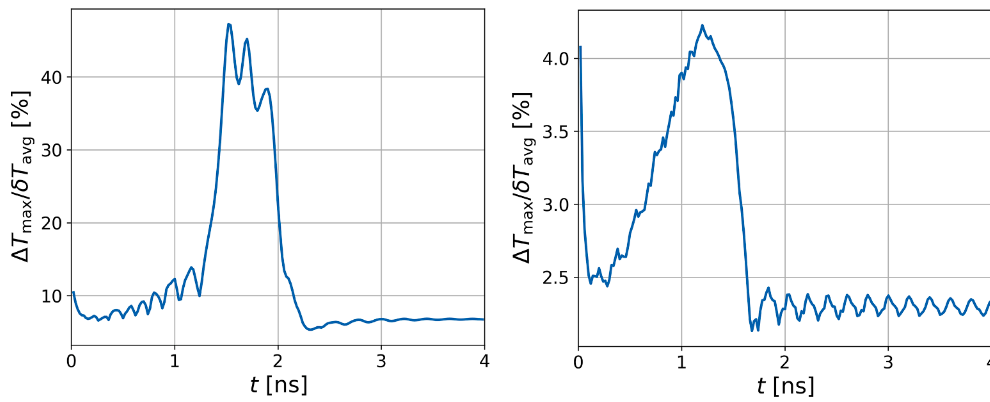

Fig. 9. Ratio of the maximum temperature difference ΔT_{max} of the FL to the average FL temperature increase δT_{avg} for structures with broadened contacts and SiO_2 passivation layer. The structure with MTJ diameter of 40 nm (20 nm) is shown on the left (right). Due to the passivation, ΔT_{max} is increased and exceeds 45 % of the average FL temperature increase for the wide MTJ, whereas it stays below 5% for the narrower MTJ.

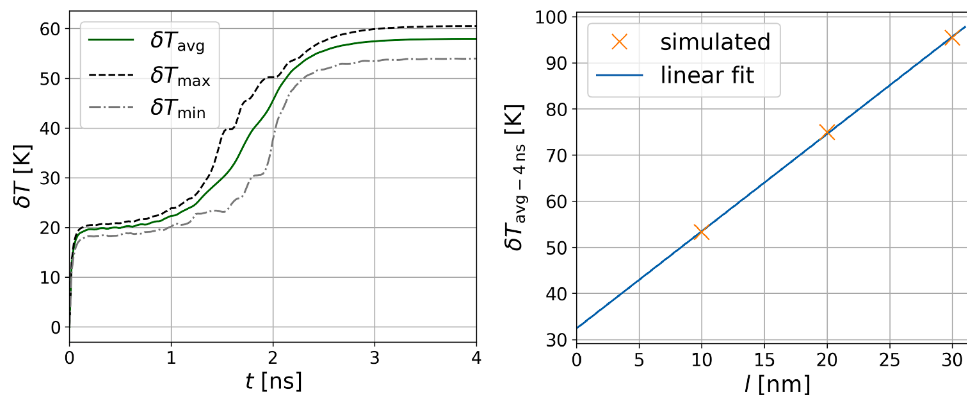

Fig. 10. Left) Temperature increase in the FL for a structure from Fig. 2 with the FL thermal conductivity reduced to 10 % of the original value. ΔT_{max} exceeds 50 % of δT_{avg} during the fast switching phase (not shown). Right) An average temperature increase for the increasing length of the narrow contact part at 4 ns. The average temperature increases linearly with the increasing contact length.

original value and therefore is not shown.

4. Conclusion

We have employed a fully 3D finite element model, coupling heat, charge, and spin transport to magnetization dynamics in order to study the FL temperature development in STT-MRAM during switching. At the beginning of the P-AP switching, the FL temperature reaches higher values than those for the AP-P switching, which will accelerate the initial switching phase. We also confirmed that a strong temperature inhomogeneity is developed across the FL, originating from the inhomogeneous current density due to non-uniform magnetization in a cylindrical STT-MRAM with a diameter of 40 nm. The ratio of the maximum temperature difference to the average temperature increase at the FL exceeds 30% for the simple five-layer structure in the rapid switching phase. While the maximum and minimum FL temperature cannot be reproduced using an average potential and current density across the FL, the average FL temperature coincides with the results of the fully 3D model.

When broadened contacts and a passivation layer are considered, the temperature variation in the FL with a diameter of 40 nm further increases due to some additional cooling at the FL edges caused by the passivation layer. The edge cooling will be further increased when a passivation material with a higher thermal conductivity, such as Si_3N_4, is used. The FL thermal conductivity reduction increases the temperature inhomogeneity in the FL even further, whereas a prolongation of the contacts only results in a linear increase of the absolute FL temperature. In the MTJ with a diameter of 20 nm, however, the temperature variation in the FL is strongly reduced. This suggests that a simpler 1D current model may be used with sufficient accuracy to calculate the FL temperature for MTJs with smaller diameters.

As the heat flux from the FL increases, when broad contacts and a passivation layer are used, the introduction of an additional insolation oxide layer between the MTJ and the contact may be desirable to trap the heat produced in the FL to facilitate the switching. However, this has to be done with caution as it will slow down the cooling of the FL, which may compromise the retention due to a possible data loss after writing.

Declaration of Competing Interest

The authors declare that they have no known competing financial interests or personal relationships that could have appeared to influence the work reported in this paper.

Acknowledgements

Financial support by the Austrian Federal Ministry for Digital and Economic Affairs, the National Foundation for Research, Technology and Development, and the Christian Doppler Research Association is gratefully acknowledged. The authors acknowledge TU Wien Bibliothek for financial support through its Open Access Funding Program.

References

[1] Ohno H. A hybrid CMOS/magnetic tunnel junction approach for non-volatile integrated circuits. In: 2009 Symposium on VLSI Technology (VLSI Technology); 2009. p. 122–3.

[2] Wang KL, Amiri PK. Nonvolatile spintronics: perspectives on instant-on nonvolatile nanoelectronic systems. SPIN 2012;02(02):1250009. https://doi.org/10.1142/S2010324712500099.

[3] Joshi VK, Barla P, Bhat S, Kaushik BK. From MTJ device to hybrid CMOS/MTJ circuits: A review. IEEE Access 2020;8:194105–46. https://doi.org/10.1109/ACCESS.2020.3033023.

[4] Suzuki D, Natsui M, Mochizuki A, Miura S, Honjo H, et al. Fabrication of a 3000–6-input-LUTs embedded and block-bevel power-gated non-volatile FPGA chip using p-MTJ-based logic-in-memory structure. In: 2015 Symposium on VLSI Circuits (VLSI Circuits); 2015. C172–3. https://doi.org/10.1109/VLSIC.2015.7231371.

[5] Thomas L, Jan G, Zhu J, Liu H, Lee Y-J, Le S, et al. Perpendicular spin transfer torque magnetic random access memories with high spin torque efficiency and thermal stability for embedded applications (invited). J Appl Phys 2014;115(17):172615. https://doi.org/10.1063/1.4870917.

[6] Cubukcu M, Boulle O, Drouard M, Garello K, Onur Avci C, Mihai Miron I, et al. Spin-orbit torque magnetization switching of a three-terminal perpendicular magnetic tunnel junction. Appl Phys Lett 2014;104(4):042406. https://doi.org/10.1063/1.4863407.

[7] Prejbeanu IL, Kerekes M, Sousa RC, Sibuet H, Redon O, Dieny B, et al. Thermally assisted MRAM. J Phys: Condens Matter 2007;19(16):165218. https://doi.org/10.1088/0953-8984/19/16/165218.

[8] Taniguchi T, Imamura H. Thermally assisted spin transfer torque switching in synthetic free layers. Phys Rev B 2011;83(5). https://doi.org/10.1103/PhysRevB.83.054432.

[9] Gapihan E, Hérault J, Sousa RC, Dahmane Y, Dieny B, Vila L, et al. Heating asymmetry induced by tunneling current flow in magnetic tunnel junctions. Appl Phys Lett 2012;100(20):202410. https://doi.org/10.1063/1.4719663.

[10] Hadámek T, Selberherr S, Goes W, Sverdlov V. Heating asymmetry in magnetoresistive random access memories. Proceedings of the World Multi-Conference on Systemics, Cybernetics and Informatics (WMSCI), in press. 2021.

[11] Fiorentini S, Ender J, Selberherr S, de Orio RL, Goes W, Sverdlov V. Coupled spin and charge drift-diffusion approach applied to magnetic tunnel junctions. Solid-State Electron 2021;186:108103. https://doi.org/10.1016/j.sse.2021.108103.

[12] Fiorentini S, Ender J, Mohamedou M, Orio R, Selberherr S, et al. Computation of torques in magnetic tunnel junctions through spin and charge transport modeling. In: 2020 International Conference on Simulation of Semiconductor Processes and Devices (SISPAD); 2020. p. 209–12. https://doi.org/10.23919/SISPAD49475.2020.9241657.

[13] Abert C, Ruggeri M, Bruckner F, Vogler C, Hrkac G, Praetorius D, et al. A three-dimensional spin-diffusion model for micromagnetics. Sci Rep 2015;5(1). https://doi.org/10.1038/srep14855.

[14] Aurélio D, Torres L, Finocchio G. Magnetization switching driven by spin-transfer-torque in high-TMR magnetic tunnel junctions. J Magn Magn Mater 2009;321(23):3913–20. https://doi.org/10.1016/j.jmmm.2009.07.050.

[15] Deschenes A, Muneer S, Akbulut M, Gokirmak A, Silva H. Analysis of self-heating of thermally assisted spin-transfer torque magnetic random access memory. Beilstein J Nanotechnol 2016;7(1):1676–83. https://doi.org/10.3762/bjnano.7.160.

[16] Hadámek T, Bendra M, Fiorentini S, Ender J, de Orio RL, et al. "Temperature increase in MRAM at writing: A finite element approach. In: 2021 Joint International EUROSOI Workshop and International Conference on Ultimate Integration on Silicon (EuroSOI-ULIS); 2021. p. 1–4. https://doi.org/10.1109/EuroSOI-ULIS53016.2021.9560669.

[17] Jang H, Marnitz L, Huebner T, Kimling J, Kuschel T, Cahill DG. Thermal Conductivity of Oxide Tunnel Barriers in Magnetic Tunnel Junctions Measured by Ultrafast Thermoreflectance and Magneto-Optic Kerr Effect Thermometry. Phys Rev Appl 2020;13(2). https://doi.org/10.1103/PhysRevApplied.13.024007.

[18] Fredkin DR, Koehler TR. Hybrid method for computing demagnetizing fields. IEEE Trans Magn 1990;26(2):415–7. https://doi.org/10.1109/20.106342.

[19] Anderson R, Andrej J, Barker A, Bramwell J, Camiera J-S, et al. MFEM: A modular finite element library. Comput Math Appl 2021;81:42–74. https://doi.org/10.1016/j.camwa.2020.06.009.

[20] Oezelt H, Kovacs A, Fischbacher J, Bance S, Gubbins M, Schrefl T. Transition jitter in heat assisted magnetic recording by micromagnetic simulation. IEEE Trans Magn 2017;53(11):1–5. https://doi.org/10.1109/TMAG.2017.2709840.

[21] Hahn MB. Temperature in micromagnetism: cell size and scaling effects of the stochastic Landau–Lifshitz equation. J Phys Commun 2019;3(7):075009. https://doi.org/10.1088/2399-6528/ab31e6.

[22] Hayakawa J, Ikeda S, Lee YM, Sasaki R, Meguro T, Matsukura F, et al. Current-Induced Magnetization Switching in MgO Barrier Based Magnetic Tunnel Junctions with CoFeB/Ru/CoFeB Synthetic Ferrimagnetic Free Layer. Jpn J Appl Phys 2006;45(No. 40):L1057–60.

Tomáš was born in Opava, Czech Republic, in 1992. He received his Bachelor degree in Mechatronics from Brno University of Technology in 2015. After an exchange year at the Norwegian University of Science and Technology, Norway, he enrolled in a Master program therein, receiving his Master's degree (MSc) in Physics in November 2018. In addition to his expertise in condensed-matter physics, Tomáš has previous experience working in the fields of numerical acoustics and robotics. Tomáš joined the Christian Doppler Laboratory on Nonvolatile Magnetoresistive Memory and Logic in July 2020, where has been working towards his doctoral degree. His main focus is on numerical simulations of heat production, transport and thermal effects in the magnetoresistive memories.